

Structural properties of charge disproportionation and magnetic order in $\text{Sr}_{2/3}\text{Ln}_{1/3}\text{FeO}_3$ (Ln=La, Pr, and Nd)

Javier Blasco,^{1,*} J. Alberto Rodríguez-Velamazán,² Joaquín García,¹ Gloria Subías,¹ Cristina Piquer,¹ Vera Cuartero,³ M. Concepción Sánchez,¹ and Jolanta Stankiewicz¹

¹*Instituto de Ciencia de Materiales de Aragón, Departamento de Física de la Materia Condensada, CSIC-Universidad de Zaragoza. C/ Pedro Cerbuna 12, 50009 Zaragoza, Spain*

²*Institut Laue-Langevin, Grenoble Cedex 38042, France*

³*Centro Universitario de la Defensa, Carretera de Huesca s/n, 50090 Zaragoza, Spain*



(Received 20 July 2018; published 18 September 2018)

The structural properties and the magnetic ground state of $\text{Sr}_{2/3}\text{Ln}_{1/3}\text{FeO}_3$ (Ln = La, Pr, Nd) samples were studied by means of synchrotron x-ray powder diffraction, neutron powder diffraction, and Mössbauer spectroscopy. All samples exhibit a metal-insulator-like transition coupled to a magnetic arrangement at a critical temperature, T_{MI} . The diffraction techniques reveal strong structural changes at T_{MI} that lead to new cells with reduced symmetry at low temperature. The new symmetry of the low-temperature phase has been determined for all compounds. The space groups are $P\bar{3}c1$ for La-based compound and $A2/n$ for the rest of samples. The high-resolution x-ray patterns detected superstructure peaks that can be accounted for by a small charge disproportionation between two nonequivalent Fe sites in the low-temperature phase explained in terms of a charge density wave that propagates along one of the body diagonals of the primitive cubic cell of these compounds. Our results clearly reveal that a full charge disproportionation of Fe^{4+} into Fe^{3+} and Fe^{5+} is not produced. We have determined the magnetic ordering of these samples exhibiting an antiferromagnetic structure with a sixfold periodicity with respect to the primitive cubic structure. The magnetic group accounting for the magnetic arrangements was obtained by a symmetry analysis and it is $C2/c$ (15.85) for all samples but with different unit cell depending on the type of FeO_6 tilts. The collinear ordering of Fe moments is established perpendicular to the charge density wave (along the body diagonal of the primitive cubic cell) and also perpendicular to the unique monoclinic axis.

DOI: [10.1103/PhysRevB.98.104422](https://doi.org/10.1103/PhysRevB.98.104422)

I. INTRODUCTION

The close relationship between the charge order (CO) and the metal-insulator transition (MIT) has been studied in a multitude of metal transition oxides and their properties are still a matter of discussion [1–5]. In this field, mixed-valence Fe oxides exhibit a rich variety of examples [5–10], including magnetite, YFe_2O_4 , or $\text{Sr}_{2/3}\text{Ln}_{1/3}\text{FeO}_3$ (Ln = La, Pr, or Nd) that show changes in resistivity of more than one order of magnitude at the critical temperature, T_{MI} . Traditionally, the MIT has been understood as the transition from a high-temperature phase ($T > T_{\text{MI}}$), with a high electrical conductivity due to fast electron hopping between equivalent Fe atoms, to an insulating phase below T_{MI} , where the electrons are localized at specific Fe sites. In the case of magnetite or YFe_2O_4 , Fe^{2+} and Fe^{3+} are randomly distributed in the crystal lattice above T_{MI} , while a regular pattern is established below T_{MI} giving rise to a CO transition. However, recent crystallographic and spectroscopic studies are challenging this traditional interpretation as a full CO has not been observed in these compounds. High-resolution x-ray diffraction studies using synchrotron radiation have revealed that a bimodal distribution of two types of cations (namely $\text{Fe}^{2+}/\text{Fe}^{3+}$) is

quite unusual in these compounds. In magnetite for instance [11], the low-temperature phase can be refined in the nonpolar space group $C2/c$ with ten nonequivalent octahedral irons with small differences in their local environments and charges ranging between 2.53 and 2.84. This result agrees with the small charge disproportionation obtained from resonant x-ray scattering experiments (RXS) [12]. Similarly, YFe_2O_4 has a complicated distorted structure at low temperature with 49 nonequivalent Fe sites and RXS revealed a maximum charge disproportionation of $0.5 e^-$ among the different sites [13].

$\text{Sr}_{1-x}\text{La}_x\text{FeO}_{3-\delta}$ is a family of mixed ionic and electronic conductors as these materials have aliovalent doping and oxygen nonstoichiometry [14,15]. These properties make them useful as cathode material for protonic ceramic fuel cells [16] and its utility is enhanced by the feasibility of growing thin films [17]. $\text{Sr}_{2/3}\text{Ln}_{1/3}\text{FeO}_3$ is a particular case that has received great attention due to the occurrence of MITs coupled to a charge disproportionation (CD) in the Fe sublattice and the subsequent CO includes the arrangement of Fe^{3+} and Fe^{5+} cations. The MIT opens the possibility of developing robust low-power and high speed transistors [18]. Above T_{MI} , the iron is in a mixed valence state, $\text{Fe}^{+3.67}$ but at low temperature the CD ($2\text{Fe}^{4+} \rightarrow \text{Fe}^{3+} + \text{Fe}^{5+}$) leads to a bimodal distribution of Fe^{3+} and Fe^{5+} cations with the ratio 2:1. This model explained results from Mössbauer spectroscopy of $\text{Sr}_{2/3}\text{La}_{1/3}\text{FeO}_3$ below $T_{\text{MI}} \sim 200$ K that found two types

*jbc@unizar.es

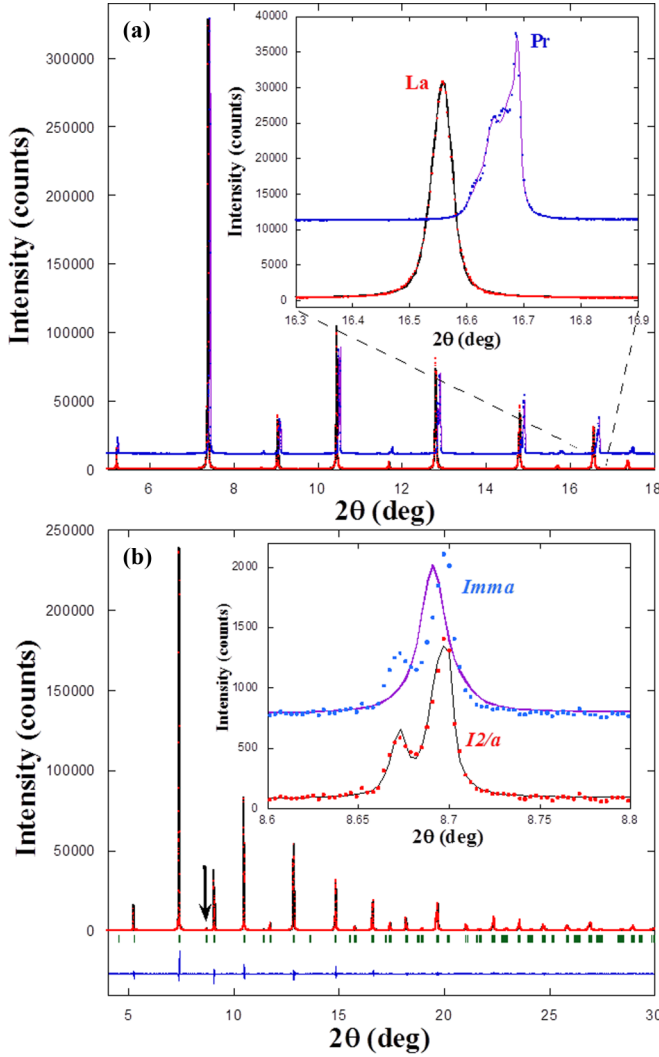


FIG. 1. (a) X-ray patterns at 295 K for $\text{Sr}_{2/3}\text{La}_{1/3}\text{FeO}_3$ and $\text{Sr}_{2/3}\text{Pr}_{1/3}\text{FeO}_3$. Inset: Detail of different peak splitting. (b) Rietveld analysis of x-ray diffraction pattern for $\text{Sr}_{2/3}\text{Nd}_{1/3}\text{FeO}_3$ at 295 K. The arrow indicates the peaks of the inset with two possible refinements.

possible modes of octahedral tilting and the resulting distorted structures have been studied by different authors in the past [32–34]. Details about the distortions induced by cooperative tilting of BO_6 octahedra related to the compounds of this study can be found in the Supplemental Material [31].

Figure 1 shows the x-ray patterns at room temperature of the three $\text{Sr}_{2/3}\text{Ln}_{1/3}\text{FeO}_3$ compounds. As reported previously [9,10,20], $\text{Sr}_{2/3}\text{La}_{1/3}\text{FeO}_3$ shows a rhombohedral distortion that can be accounted for by the tilting system $a^-a^-a^-$ according to the Glazer notation [32]. The hexagonal lattice parameters are related to the primitive cubic cell by the following lattice vectors: $\mathbf{a}_h = (1\ 0\ -1)$, $\mathbf{b}_h = (-1\ 1\ 0)$ and $\mathbf{c}_h = (2\ 2\ 2)$. The patterns of this compound exhibit anisotropic peak broadening revealing either anisotropic crystal size or the occurrence of intrinsic microstrain. The sharpest peaks correspond to the $(0, 0, l)$ reflections, suggesting a needle-like shape of the crystallites. This anisotropic broadening was accounted for in the structural refinements using the

TABLE I. Structural parameters at room temperature obtained from the refinement of high-resolution x-ray data (space group, lattice constants, fractional coordinates, temperature factors, average Fe-O bond lengths, average Fe-O-Fe bond angles, and reliability factors defined as in Ref. [26]). Atoms are located in the $R\bar{3}c$ ($I2/a$) space group as follows: Sr/Ln at $6a$: $0, 0, \frac{1}{4}(4e : \frac{1}{4}, y, 0)$; Fe at $6b$: $0, 0, 0(4b : 0, \frac{1}{2}, 0)$; O1 at $18e$: $x, 0, \frac{1}{4}(4e : \frac{1}{4}, y, 0)$; and O2 at $8f$: x, y, z .

Sample (Ln)	La	Pr	Nd
<i>Space group</i>	$R\bar{3}c$	$I2/a$	$I2/a$
\mathbf{a} (Å)	5.4864(2)	7.7158(3)	7.7140(1)
\mathbf{b} (Å)	–	5.4829(2)	5.4814(1)
\mathbf{c} (Å)	13.4101(6)	5.4579(2)	5.4561(1)
β (deg)	–	90.041(1)	90.044(1)
Vol/Z (Å ³)	58.26(2)	57.72(1)	57.67(1)
Coordinates			
$\mathbf{R}:x$	0	$\frac{1}{4}$	$\frac{1}{4}$
y	0	–0.0001(3)	–0.0006(2)
z	$\frac{1}{4}$	0	0
B (Å ²)	0.28(1)	0.52(1)	0.58(1)
Fe: B (Å ²)	0.05(1)	0.31(1)	0.32(1)
$\mathbf{O1}:x$	0.4816(4)	$\frac{1}{4}$	$\frac{1}{4}$
y	0	0.4675(20)	0.4580(9)
z	$\frac{1}{4}$	0	0
B (Å ²)	0.87(2)	1.38(18)	1.47(12)
$\mathbf{O2}:x$	–	0.4831(6)	0.4826(5)
y	–	0.7401(25)	0.7464(25)
z	–	0.2599(18)	0.2539(29)
B (Å ²)	–	0.68(8)	1.25(6)
(Fe-O) (Å)	1.941(1)	1.939(4)	1.939(5)
(Fe-O-Fe) (deg)	174.0(1)	171.2(3)	170.1(2)
Valence	3.67(1)	3.71(4)	3.71(5)
$R_{\text{wp}}/R_{\text{Bragg}}$ (%)	8.7/2.5	10.5/4.5	9.1/2.1

phenomenological model proposed by Stephens [35], which has been implemented in the Fullprof software [26].

Although an analogous trigonal structure was reported for $\text{Sr}_{2/3}\text{Pr}_{1/3}\text{FeO}_3$ and $\text{Sr}_{2/3}\text{Nd}_{1/3}\text{FeO}_3$ [36,37], we observe significant splitting of several peaks, suggesting an orthorhombic distortion [see Fig. 1(a)]. In a previous work using a laboratory diffractometer, we tentatively refined their structures using the space group $Imma$ in agreement with the $a^-a^-c^0$ tilting system [38]. Similar structure was reported for $\text{Sr}_{1/2}\text{Pr}_{1/2}\text{FeO}_3$ in Ref. [39]. However, in the present study using high-resolution XRD data, we were able to observe that a monoclinic cell improves the refinement and we detected small superstructure peaks associated to the tilts of FeO_6 octahedra confirming this point as can be seen in the Fig. 1(b). Therefore, the actual unit cell for these compounds adopts the $I2/a$ space group following the $a^-a^-c^-$ tilting system with a small out-of-phase rotation of the FeO_6 octahedra along the cubic c axis [31]. The relationship between the distorted monoclinic cell and the primitive cubic cell follows these lattice vectors: $\mathbf{a}_m = (0\ 0\ 2)$, $\mathbf{b}_m = (1\ 1\ 0)$, and $\mathbf{c}_m = (-1\ 1\ 0)$. The structural parameters obtained from the refinements are summarized in the Table I. Overall, the unit cell parameters decrease as the rare-earth size does (following the lanthanide contraction).

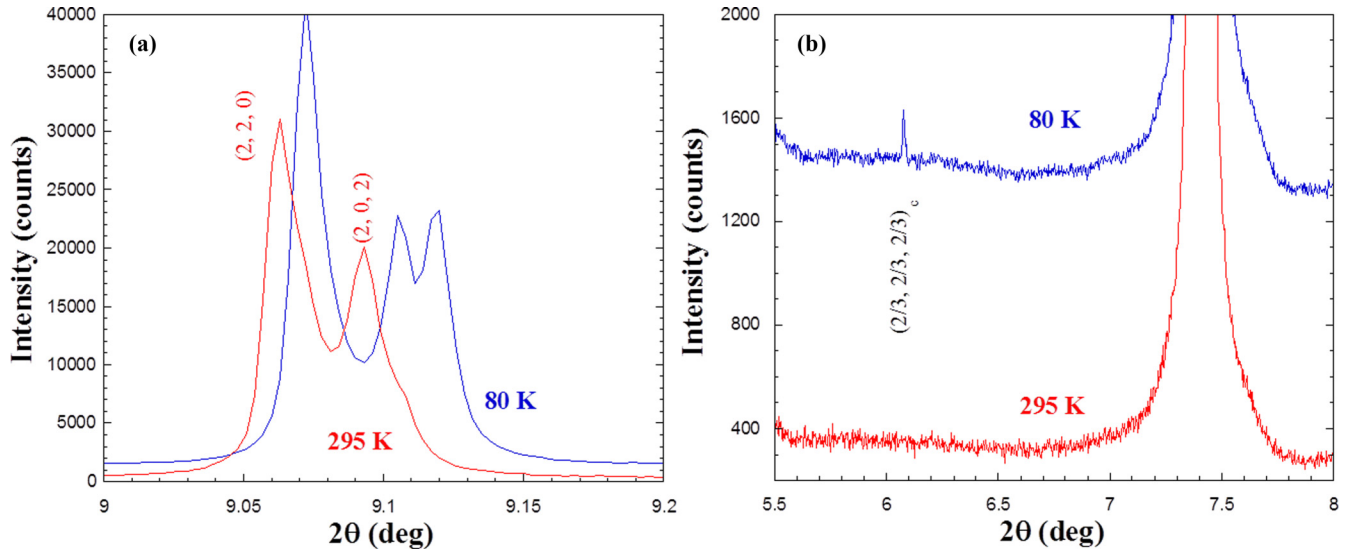


FIG. 2. Selected regions of x-ray patterns collected at 295 and 5 K for $\text{Sr}_{2/3}\text{Nd}_{1/3}\text{FeO}_3$ to compare (a) the peak splitting and (b) the occurrence of new superstructure peaks indexed in the frame of the primitive cubic cell.

The Fe-O bond lengths estimated from the refined fractional coordinates show similar values for the three compounds. In fact, the Fe valence inferred from the bond valence analysis ranges between 3.67 and 3.71 in excellent agreement with the nominal value expected from the Ln/Sr ratio.

Upon cooling below the MIT, two types of changes are perceptible in the x-ray patterns of the three samples as illustrated in Fig. 2 for the Nd-based compound. First, some diffraction peaks are split indicating a sudden change in the unit cell dimensions. Second, the occurrence of new superstructure peaks following the propagation vector $k = (1/3, 1/3, 1/3)$ respect to the primitive cubic cell and differentiating one of its body diagonals. These new reflections are very weak and very hardly detectable by conventional laboratory diffractometers (see Fig. 2). For instance, the intensity ratio between the first superstructure peak $(2/3, 2/3, 2/3)$ and the most intense peak in the pattern is around 3.7×10^{-4} . According to reported group-theory analysis [40], the cation ordering pattern associated to the previous propagation vector can be accounted for by the condensation of modes belonging to the irreducible representation (Irrep) LD1 with the order parameter $(a, 0, 0, 0, 0, 0)$. The result of this distortion splits both the A- and B-sites and the nominal formula of the distorted structure may be seen as $\text{A}_2\text{A}'\text{B}_2\text{B}'\text{O}_9$. In the case of $\text{Sr}_{2/3}\text{La}_{1/3}\text{FeO}_3$ compound, the combination of the cation ordering and the $a^-a^-a^-$ octahedral system leads to a primitive triclinic cell with $P\bar{3}c1$ space group [31,40]. Both cells, $R\bar{3}c$ and $P\bar{3}c1$, have the same lattice parameters and the Fe atoms located at the Wyckoff position $6(c)$ in the $R\bar{3}c$ cell are split into two orbits Fe1 and Fe2 located at the Wyckoff positions $2(b)$ and $4(d)$ in the $P\bar{3}c1$ cell. In the same way, Sr(La) is also split. Sr(La)1 and Sr(La)2 are placed at the Wyckoff positions $2(a)$ and $4(d)$. Fe2 and Sr(La)2 have the only possibility of shifting along the z direction in the hexagonal cell (or body diagonal in the rhombohedral setting). The occurrence of superstructure peaks is due to subtle atom shifts. In fact, accurate fits can be obtained with the atom fractional coordinates of the high temperature phase but that model is unable to account for the

new weak superstructure peaks. The refinement of fractional coordinates yields different results depending on the starting values. This is a strong indication about the existence of several local minima in the fit procedure. To gain insights into the structural distortion of the low-temperature phase, we have taken full advantage of the refinements using modes amplitudes [29]. The intensity in the superstructure peaks appears by condensation of the LD1 modes associated to the vector $\mathbf{k} = (1/3, 1/3, 1/3)$. There are four possibilities (or atom shifts) giving rise to similar satellite peaks. They are displayed in the Fig. 3 using the program VESTA [41]. The common ingredient for all cases is the shift of Fe2 and Sr(La)2 atoms in opposite directions along the hexagonal z axis. In addition, the O2 atoms located at $12(g)$ position also move coupled to the Sr(La)2 in the same direction along the z axis but these atoms have more degrees of freedom and they have also shifted in the xy plane. Depending on their modes amplitudes, the O2 approaches to either Fe (models 1 and 2) or Sr (models 3 and 4) atoms and the consequences are different. In the first cases, CD occurs in the Fe sites while in the other two models different oxidation states are observed in the Sr(La) sites. As RXS resonance is clearly observed at the Fe K-edge [23], models 3 and 4 can be discarded, while models 1 and 2 would yield similar RXS reflections and opposite sequences for the CD in the Fe-sublattice. The CD would be $-\text{Fe}^{3.67+\delta} - \text{Fe}^{3.67-\delta'} - \text{Fe}^{3.67-\delta'}$ — and $-\text{Fe}^{3.67-\delta} - \text{Fe}^{3.67+\delta'} - \text{Fe}^{3.67+\delta'}$ — for models 1 and 2, respectively. Both refinements yield similar reliability factors so x-ray diffraction cannot give a definitive conclusion. Previous hypothesis assumed a full CD of the type: $2\text{Fe}^{4+} \rightarrow \text{Fe}^{3+} + \text{Fe}^{5+}$ [19]. This premise might agree with the model 1 if $\delta = 1.33$ and $\delta' = 0.67$. However, the bond valence sum (BVS) of our refinements yields a difference of 0.4 valence units between both sites in any of the two models. This partial CD is in agreement with the RXS study reported in Ref. [23]. In model 1, our result is much closer to the presence of Fe^{4+} at the Wyckoff position $2(b)$ and an even mixture of Fe^{3+} and Fe^{4+} at position $4(d)$ in accord with x-ray absorption

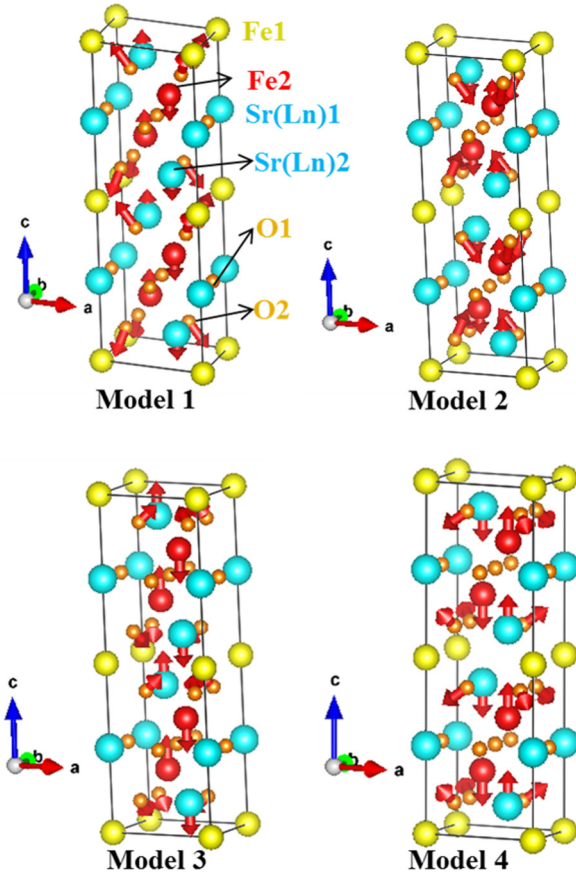


FIG. 3. Possible atomic shifts for Fe2, Sr(Ln)2 and O2 atoms associated to the condensation of modes from the Irrep LD1. The four models give rise to $(h/3, h/3, h/3)_c$ superstructure peaks but only models 1 and 2 yield a RXS signal at the Fe K-edge.

spectroscopy [10]. Moreover, this model is more in agreement with the results obtained from the Mössbauer spectroscopy (see below). Figure 4 shows the Rietveld analysis at 80 K

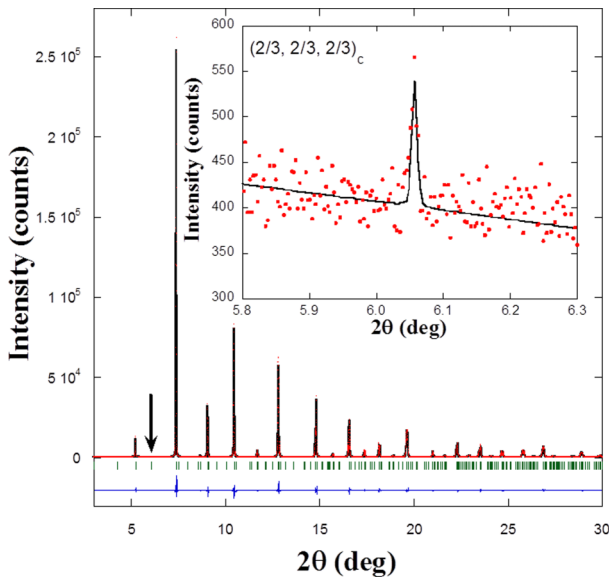


FIG. 4. Rietveld analysis of the high-resolution x-ray diffraction pattern for $\text{Sr}_{2/3}\text{La}_{1/3}\text{FeO}_3$. The arrow indicates the region emphasized in the inset with the first superstructure $(h/3, h/3, h/3)_c$ peak.

TABLE II. Structural parameters at 80 K obtained from the refinement of high-resolution x-ray data (space group, lattice constants, fractional coordinates, temperature factors, and reliability factors defined as in Ref. [26]). Atoms are located in the $P\bar{3}c1$ ($A2/n$) space group as follows: Sr/Ln1 at $2a:0, 0, \frac{1}{4}$ ($4e:3/4, y, 3/4$); Sr/Ln2 at $4d:1/3, 2/3, z$ ($8f: x, y, z$); Fe1 at $2b:0, 0, 0$ ($4c:0, 1/4, 1/4$); Fe2 at $4d:1/3, 2/3, z$ ($8f: x, y, z$); O1 at $6f: x, 0, \frac{1}{4}$ ($4e:3/4, y, 3/4$); and O2 at $12g: x, y, z$ (rest of O at $8f: x, y, z$).

Sample (Ln)	La	Pr	Nd
<i>space group</i>	$P\bar{3}c1$	$A2/n$	$A2/n$
a (Å)	5.48156(1)	13.34887(5)	13.32419(3)
b (Å)	—	5.44397(2)	5.48041(1)
c (Å)	13.37082(3)	9.49920(3)	9.43490(2)
β (deg)	—	89.5822(2)	90.0569(1)
Sr/Ln1:y	0	0.7480(12)	0.7509(9)
Sr/Ln2:x	1/3	0.9163(2)	0.9172(2)
y	2/3	0.7514(8)	0.7462(5)
z	0.9174(2)	0.0826(2)	0.0835(4)
B_{Sr} (Å ²)	0.23(2)	0.16(2)	0.26(4)
Fe1: B_{Fe} (Å ²)	0.17(4)	0.17(6)	0.17(7)
(Fe1 -O) (Å)	1.912(3)	1.929(9)	1.923(7)
BVS-Fe1	3.96(3)	3.80(9)	3.87(7)
Fe2: x	1/3	0.1668(4)	0.1680(4)
y	2/3	0.7467(17)	0.7482(14)
z	0.1680(3)	0.0761(4)	0.0824(7)
(Fe2 -O) (Å)	1.956(3)	1.949(9)	1.951(6)
BVS-Fe2	3.53(3)	3.62(9)	3.58(7)
O1: x	0.518(2)	0.75	0.75
y	0	0.273(4)	0.299(6)
O2: x	0.1955(14)	0.9334(17)	0.9198(13)
y	0.8664(14)	0.536(4)	0.512(3)
z	0.813(4)	0.322(2)	0.3143(18)
O3: x	—	0.254(2)	0.2392(16)
y	—	0.533(5)	0.503(4)
z	—	-0.021(3)	-0.024(2)
O4: x	—	0.4165(17)	0.4273(13)
y	—	0.481(4)	0.509(3)
z	—	0.344(2)	0.3381(18)
O5: x	—	0.9155(17)	0.9124(13)
y	—	0.229(3)	0.209(3)
z	—	0.081(2)	0.0834(19)
B_{O} (Å ²)	0.48(2)	0.76(7)	0.19(4)
$R_{\text{wp}}/R_{\text{Bragg}}$ (%)	7.0/1.8	10.7/4.1	8.2/2.5

for $\text{Sr}_{2/3}\text{La}_{1/3}\text{FeO}_3$ using the model 1 and in the Table II is summarized the structural parameters obtained from this refinement.

Regarding $\text{Sr}_{2/3}\text{Pr}_{1/3}\text{FeO}_3$ and $\text{Sr}_{2/3}\text{Nd}_{1/3}\text{FeO}_3$, the combination of the $a^-a^-c^-$ tilting system and cation ordering at the B-position leads to a distorted structure adopting a monoclinic cell [40], space group $A2/n$ (standard group $C2/c$), whose lattice parameters are related to the primitive cubic cell with the following vectors: $\mathbf{a}_m = (-2, -2, 2)$, $\mathbf{b}_m = (1, 0, -1)$, and $\mathbf{c}_m = (1, -2, 1)$ with an origin shift of $(1/2, -1/2, 0)$. In this case, the Fe located in the Wyckoff position $4(b)$ in the high temperature phases also splits into two orbits with positions $4(d)$ and $8(f)$. Similar

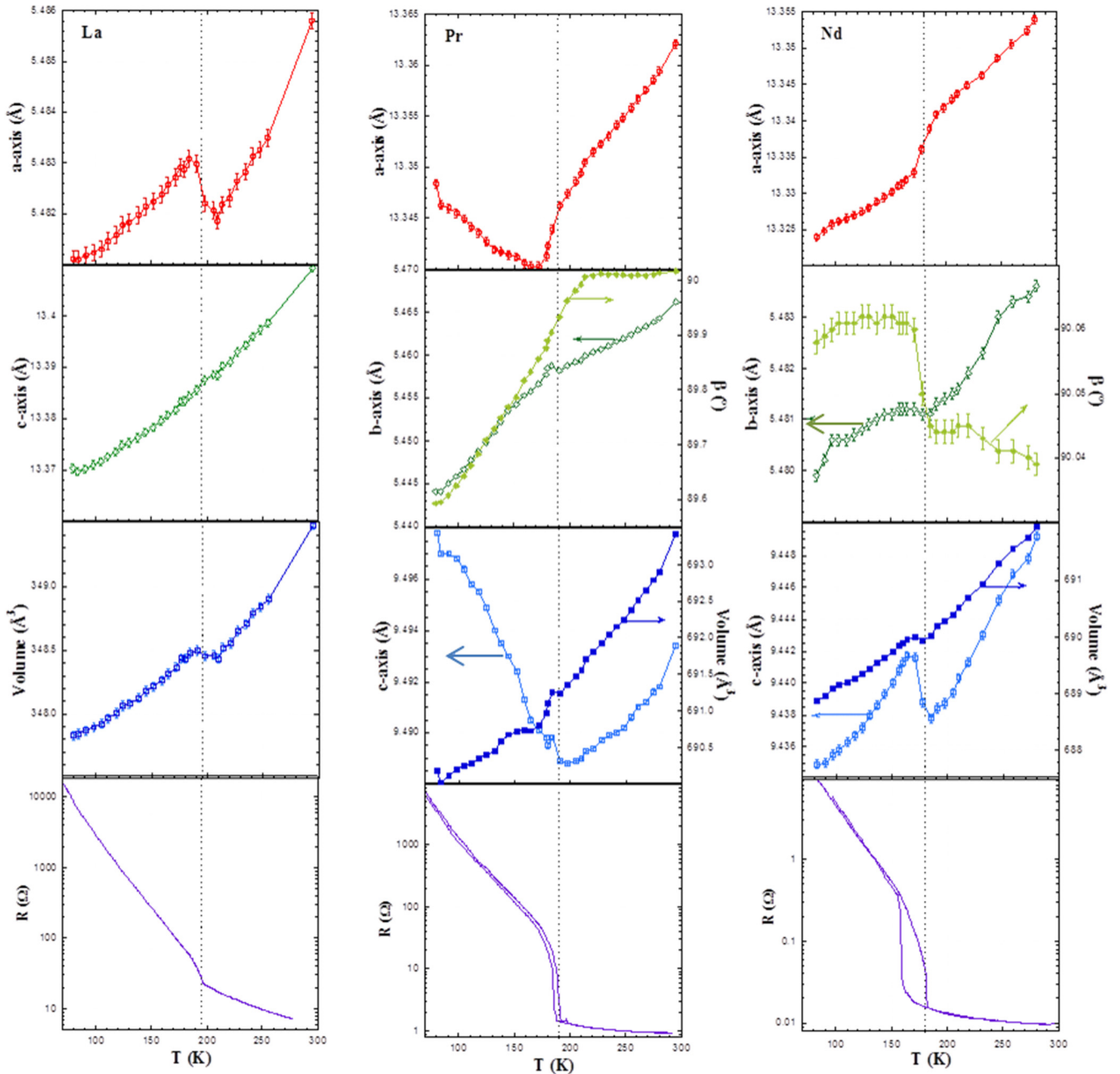


FIG. 5. Temperature dependence of refined lattice parameters from high-resolution x-ray diffraction patterns (indicated in each figure) and of electrical resistance for $\text{Sr}_{2/3}\text{La}_{1/3}\text{FeO}_3$ (left), $\text{Sr}_{2/3}\text{Pr}_{1/3}\text{FeO}_3$ (middle), and $\text{Sr}_{2/3}\text{Nd}_{1/3}\text{FeO}_3$ (right).

static frozen distortions can be obtained for both samples with analogous models of CD as observed in the La-based compound. Table II shows the refined parameters for both samples using the condensation model equivalent to model 1 in the La-based compound. The two Fe sites show a more distorted environment compared to the La-based sample but we observe a similar CD of ~ 0.4 valence units between both sites. Therefore, the three compounds show a similar CD, far below of a full disproportionation into Fe^{3+} and Fe^{5+} . It is noteworthy that the Pr-based sample exhibits the strongest monoclinic distortion at low temperature and the x-ray patterns reveal the presence of stacking faults characterized by the asymmetry of selected peaks and peak shifts out of the theoretical position.

Although a phenomenological model [28] partially solves this problem, its reliability factors in the refinements are worse compared to the other two samples (see Table II).

Figure 5 shows the temperature dependence of the lattice parameters for the three samples when heating between 80 and 300 K. The evolution of the lattice parameters is compared to the behavior of the electrical resistance, $R(T)$. The three samples show a jump in the $R(T)$ curves at T_{MI} , which slowly decreases as the Ln-size does. They do not exhibit a genuine MIT as the samples are semiconducting above T_{MI} . Overall, the jump is several orders of magnitude at T_{MI} and the hysteresis reveals a first order transition. Such a hysteresis in the $R(T)$ curves increases with decreasing the Ln-size.

Regarding the unit cell, clear changes in the lattice parameters are noticeable at T_{MI} . In the La-based sample, the most significant change is the sudden expansion ($\sim 0.025\%$) of the a axis at T_{MI} . This direction is perpendicular to the body diagonal of the primitive cubic cell and matches with the direction of the ordered magnetic moments as reported below. The c axis exhibits a monotone contraction on cooling and a kink in the temperature dependence of the unit cell volume that mirrors the abovementioned jump in the a axis. Stronger changes are observed in the monoclinic samples. Regarding the Nd-based sample, jumps in the temperature dependence of c axis and β angle are clearly visible at T_{MI} . The behavior of the former resembles the thermal dependence of the a axis in the La-sample and in fact, the monoclinic c axis is also perpendicular to the body diagonal of the primitive cubic cell. In this case the expansion at T_{MI} is a bit larger ($\sim 0.04\%$). The other two monoclinic axes are contracted with decreasing temperature but the a axis shows an inflection point at T_{MI} , whereas the b axis shows a small plateau at that temperature. Finally, the Pr-based sample shows the strongest monoclinic distortion at low temperature. The β angle begins to deviate from 90° above T_{MI} , suggesting a structural instability additional to the charge localization. This may be related to the slope change in the a axis (negative below T_{MI} and positive above it) and the continuous expansion of the c axis below T_{MI} (about 0.1% down to 80 K). It is worth noting the opposite behavior of the β angle for both monoclinic compounds using the same cell choice (same fractional coordinates). Such an angle is greater (less) than 90° for Nd-(Pr-) based sample. Summarizing, the structural changes at T_{MI} are very anisotropic in the three samples and the strongest anomalies are observed in the direction perpendicular to the diagonal of the primitive cubic cell or the direction where the CO is established. The stronger change at the MIT is observed along the c axis for both samples, suggesting a magnetostructural coupling at T_{MI} in that direction.

B. Magnetic structure of $\text{Sr}_{2/3}\text{La}_{1/3}\text{FeO}_3$

This family of compounds exhibits magnetic transitions at T_{MI} [38]. In the case of the La-based sample, its magnetic structure was previously studied using neutron powder diffraction techniques [9,20]. In both works, the magnetic structure was described using a hexagonal lattice and a propagation vector $\mathbf{k} = 0$. The symmetry of the magnetic cell is reduced to the space group $P-1$, the magnetic moments lie in the ab plane and they are antiferromagnetically ordered along the c axis following the sequence $+++- --$. This sequence can be seen as a sixfold periodicity along one pseudocubic [111] direction. The magnetic sequence agrees with a CO sequence of $\text{Fe}^{5+}\text{Fe}^{3+}\text{Fe}^{3+}\text{Fe}^{5+}\text{Fe}^{3+}\text{Fe}^{3+}$ along the abovementioned direction. The magnetic couplings are AFM for $\text{Fe}^{3+}\text{-O-Fe}^{3+}$ and $\text{Fe}^{5+}\text{-O-Fe}^{5+}$ interactions while it is FM for $\text{Fe}^{3+}\text{-O-Fe}^{5+}$ paths. Such interactions agree with the superexchange rules [42], but the refined magnetic moments disagree with a full CO disproportionation [9,20]. In addition, the exact direction of the moments is missing probably due to the presence of pseudosymmetry. Figure 6 compares neutron patterns above and below the magnetic transition. First of all, the powder neutron diffraction is not sensitive to the CD of these samples as no superstructure peaks are noticeable.

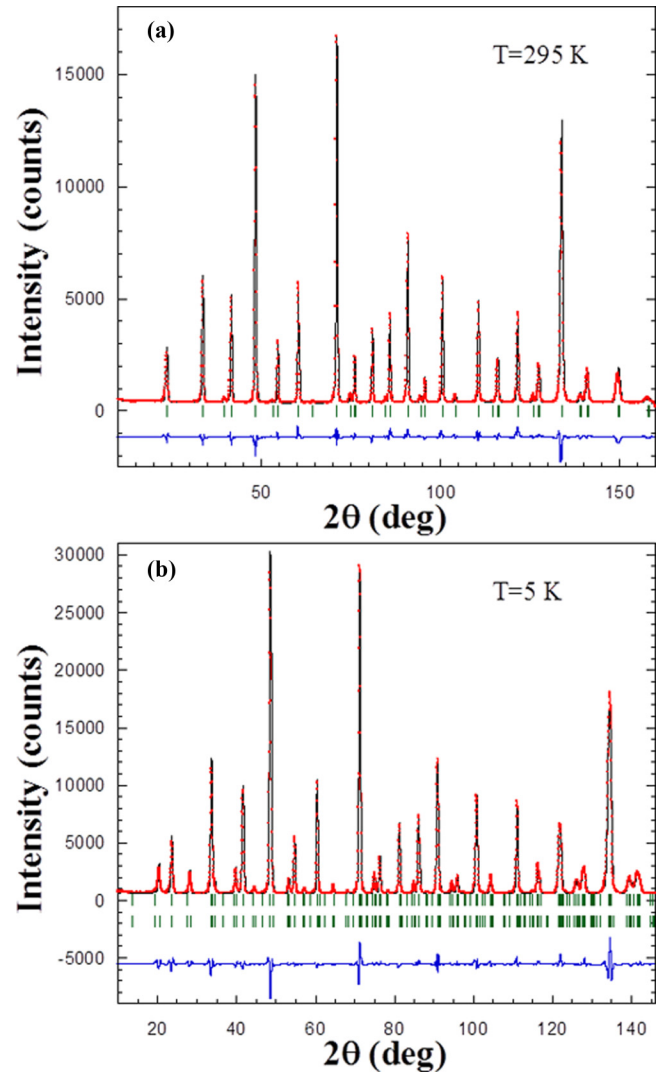


FIG. 6. Rietveld analysis of the high-resolution neutron diffraction pattern for $\text{Sr}_{2/3}\text{La}_{1/3}\text{FeO}_3$ collected at 295 K (top) and 5 K (bottom).

In fact, accurate fits can be obtained using the fractional coordinates of the undistorted phase (high-temperature phase) and only refining the magnetic contribution. Magnetic peaks are clearly seen in the patterns at low temperature and their indexation confirms that magnetic moments are in the hexagonal ab plane. In this work, we have taken full advantage of symmetry analysis to advance in the knowledge of the exact magnetic structure for this compound. For this purpose, we have used the Isodistort program [28] to explore the magnetic Irreps (mIrreps) for the nuclear cell with $P\bar{3}c1$ symmetry. The search was limited to the GM point as the propagation vector for magnetic reflections is $\mathbf{k} = 0$. The program yields six possible mIrreps: mGM1+, mGM2+, mGM3+, mGM1-, mGM2-, and mGM3-. Only mIrreps with the sign plus allow the simultaneous ordering of the two nonequivalent Fe atoms. Of these options, only mGM3+ allows the magnetic arrangement in the ab plane. In the other two mIrreps, the moments point along the c axis. Therefore, our search was focused on mGM3+. Within this mIrrep, there are three possibilities corresponding to three different magnetic

TABLE III. Magnetic structures of the AFM ordering at 5 K for $\text{Sr}_{2/3}\text{La}_{1/3}\text{FeO}_3$, $\text{Sr}_{2/3}(\text{La}_{1/2}\text{Pr}_{1/2})_{1/3}\text{FeO}_3$, $\text{Sr}_{2/3}\text{Pr}_{1/3}\text{FeO}_3$, $\text{Sr}_{2/3}(\text{Pr}_{1/2}\text{Nd}_{1/2})_{1/3}\text{FeO}_3$, and $\text{Sr}_{2/3}\text{Nd}_{1/3}\text{FeO}_3$, denoted in the table as La, LaPr, Pr, PrNd, and Nd samples, respectively. We show the magnetic space group, refined lattice constants, refined magnetic moments, and reliability factors defined as in Ref. [26]). Atoms are located in the $C2/c$ ($A2/n$) space group as follows: Sr/Ln1 at $4e$: $0, y, 1/4$ ($4e$: $3/4, y, 3/4$); Sr/Ln2 at $8f$: x, y, z ($8f$: x, y, z); Fe1 at $4a$: $0, 0, 0$ ($4c$: $0, 1/4, 1/4$); Fe2 at $8f$: x, y, z ($8f$: x, y, z); O1 at $4e$: $x, 0, 1/4$ ($4e$: $3/4, y, 3/4$); and rest of O in both cases at $8f$: x, y, z . (*) $C2/c$ transform from parent nuclear cell as $2a + b, b, c; 0, 0, 0$. $A2/n$ transform from parent as $-a, b, -c; 0, 0, 0$.

Sample (Ln)	La	LaPr	Pr	PrNd	Nd
Magnetic space group	* $C2/c$ (15.85)	$A2/n$ (15.85)	$A2/n$ (15.85)	$A2/n$ (15.85)	$A2/n$ (15.85)
Magnetic cell: a (Å)	9.4921(1)	13.3627(1)	13.3428(1)	13.2846(3)	13.2770(2)
b (Å)	5.4680(1)	5.43547(5)	5.41964(7)	5.4262(1)	5.46207(4)
c (Å)	13.3638(1)	9.43813(6)	9.44165(7)	9.4610(2)	9.3971(1)
β (deg)	90.0	89.521(1)	89.372(1)	89.772(2)	90.049(1)
Refined moments (μ_B):					
Fe1 : μ_x	2.53(8)	0	0	0	0
μ_y	0	0	0	0	0
μ_z	0	2.79(1)	2.58(7)	2.65(2)	2.25(5)
Fe2 : μ_x	3.28(1)	0	0	0	0
μ_y	0	0	0	0	0
μ_z	0	3.53(1)	3.25(4)	3.52(1)	3.32(2)
$R_{\text{wp}}/R_{\text{Bragg}}$ (%)	7.1/2.5	4.0/2.1	4.0/2.7	8.3/4.1	4.8/4.0

(Shoubnikov) groups: $C2/c$, $C2'/c'$ and $P-1$. In the two first cases, the magnetic cell is related to the crystal one in the following way: $\mathbf{a}_m = 2\mathbf{a}_h + \mathbf{b}_h$; $\mathbf{b}_m = \mathbf{b}_h$; $\mathbf{c}_m = \mathbf{c}_h$. This transformation leads to $\gamma = 90^\circ$ and $\beta \sim 90^\circ$. Exploring the magnetic groups and the possible magnetic arrangements, $P-1$ is the one with the least symmetry and it allows collinear ordering with alternate FM and AFM interactions along any crystallographic direction. This approximation was used in Ref. [9]. Thus, we are interested in the other two magnetic groups. $C2/c$ only permits the collinear order of interest ($++--$) along the \mathbf{a}_m axis whereas the $C2'/c'$ only allows this type of ordering along \mathbf{b}_m (unique axis). We have performed the refinements and we obtain that the best reliability factors were obtained for the magnetic group $C2/c$ and only 2 magnetic modes were necessary (one for each Fe position). However, the differences with the $C2'/c'$ model are very small and a study with single crystal would be necessary to achieve a definitive conclusion. The use of $P-1$ magnetic group does not improve the fit in spite of refining more parameters. In the present work, we have chosen the $C2/c$ group for two reasons. It is the magnetic group with highest symmetry that accounts for the neutron pattern of $\text{Sr}_{2/3}\text{La}_{1/3}\text{FeO}_3$ at low temperature and, second, the moments lie in the crystal axis that show more drastic changes at the magnetic transition (magnetoelastic coupling). Figure 6 shows the refinements of neutron patterns at 295 and 5 K to put forward the magnetic contribution. The magnetic data are summarized in the Table III and the magnetic structure is drawn in Fig. 7. The refined data shows two nonequivalent Fe sites whose ordered magnetic moments are 2.52 and 3.27 μ_B , values that are consistent with previous studies [9,37] and are at odd with the ones expected for Fe^{5+} and Fe^{3+} (3 and 5 μ_B) in a full CD. In the course of this research, a magnetic study on $\text{Sr}_{2/3}\text{La}_{1/3}\text{FeO}_3$ has recently been reported [43]. The results of this work are in agreement with our study showing similar conclusions about the possible magnetic groups for a collinear ordering of the Fe moments.

C. Mössbauer spectra of $\text{Sr}_{2/3}\text{La}_{1/3}\text{FeO}_3$

To gain insights into the electronic structure of Fe atoms, Mössbauer spectra of $\text{Sr}_{2/3}\text{La}_{1/3}\text{FeO}_3$ were collected at different temperatures. The Mössbauer spectra of $\text{Sr}_{2/3}\text{La}_{1/3}\text{FeO}_3$ measured between $T = 77$ and 300 K are displayed in Fig. 8. The spectra at $T = 300, 250,$ and 200 K ($T > T_{\text{MI}}$) are not magnetically split and can be perfectly fitted with a paramagnetic doublet. The corresponding linewidths, Γ ,

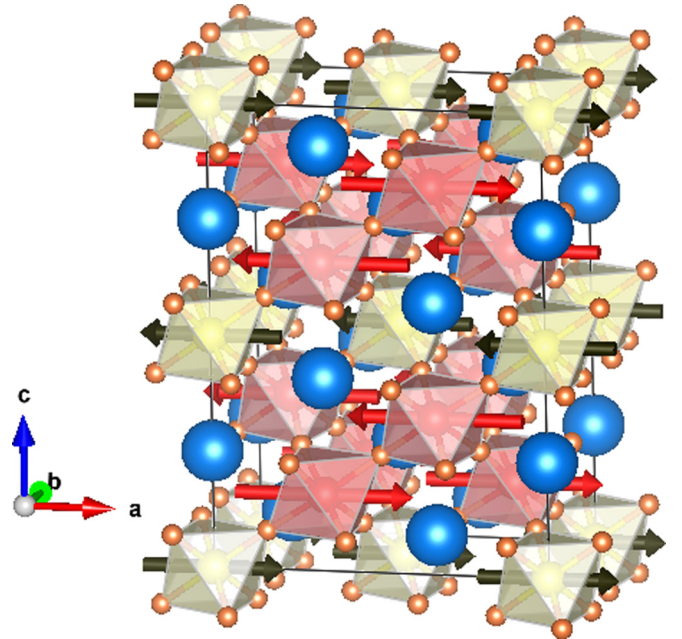


FIG. 7. Crystal and magnetic structure of $\text{Sr}_{2/3}\text{La}_{1/3}\text{FeO}_3$ at 5 K deduced from the refinement of neutron diffraction patterns and a group-theoretical analysis. The draw was produced by VESTA program [41].

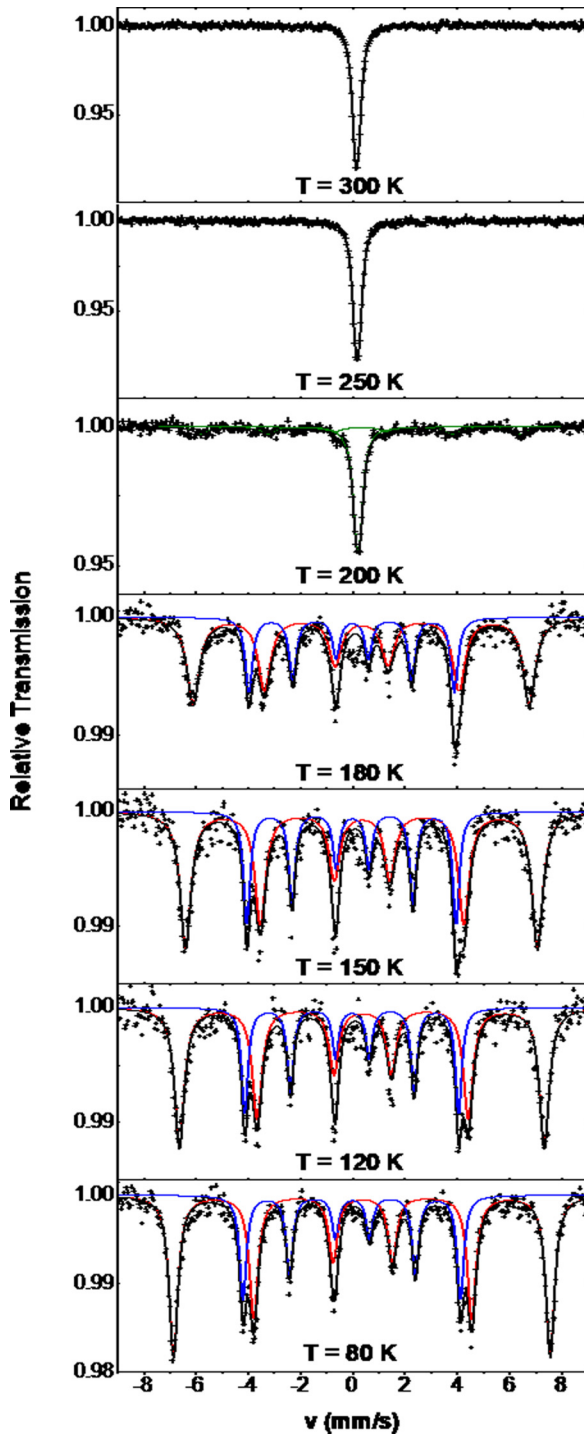


FIG. 8. Mössbauer spectra of $\text{Sr}_{2/3}\text{La}_{1/3}\text{FeO}_3$ measured between 77 and 300 K.

and hyperfine parameters (isomer shift, δ , and paramagnetic quadrupole splitting, ε) are displayed in Table IV. A small magnetic contribution is observed at $T = 200$ K (solid green line in Fig. 8). When this contribution is included in the fit, the corresponding relative intensity and hyperfine parameters are: 33%, $B_{\text{hf}} = 38$ T, $\delta = 0.307$ mms^{-1} , $\varepsilon = -0.001$ mms^{-1} , and $\Gamma = 0.66$ ms^{-1} .

Magnetic splitting is clearly observed for $T < 180$ K ($T < T_{\text{MI}}$). In this case the Mössbauer spectra consist of two superimposed sextets with intensity ratio $\approx 2:1$ (components 1 and 2, red and blue lines in Fig. 8). The parameters used in the fit, relative intensities, linewidths, hyperfine field, B_{hf} , isomer shift, and quadrupole splitting are shown in Table IV. The hyperfine field of the more intense sextet (component 1, red line in Fig. 8) is approximately twice the hyperfine field of component 2 (blue line in Fig. 8). However, they display very different isomer fields, $\delta_1 \approx 0.35$ mms^{-1} , and $\delta_2 \approx -0.03$ mms^{-1} . The thermal dependences of B_{hf} and δ are shown in Fig. 9. For $T < T_{\text{MI}}$, the weighted averages, $\langle B_{\text{hf}} \rangle = 1/3 B_{\text{hf}1} + 2/3 B_{\text{hf}2}$ and $\langle \delta \rangle = 1/3 \langle \delta_1 \rangle + 2/3 \langle \delta_2 \rangle$, are also displayed.

According to this result, Mössbauer spectroscopy agrees with the splitting of Fe atoms into two nonequivalent environments at low temperature with a rate 2:1. Moreover, the fit suggests that magnetic moments of both sites follow the rate 25:38, quite similar to the values obtained from the neutron refinement (25:33). However, with the obtained values of B_{hf} and δ is not straightforward to determine the Fe valence. To get some insight on this subject we have measured at room temperature several reference compounds belonging to the same family of compounds (see Figure S10 in the Supplemental Material [31]). According to our Mössbauer data and subsequent analysis we have observed that for these compounds the average isomer shift at RT, $\langle \delta \rangle_{\text{RT}}$, varies linearly with the Fe average valence, $\langle v_{\text{Fe}} \rangle$, (Figure S11 in the Supplemental Material) in the following manner:

$$\langle \delta \rangle_{\text{RT}} = 1.28 - 0.31 x \langle v_{\text{Fe}} \rangle. \quad (1)$$

The temperature dependence of the weighted isomer shift (Fig. 9) can be described with the well-known Debye model for the second order Doppler shift [44]. Assuming that δ_1 and δ_2 follow the same thermal dependence as $\langle \delta \rangle$, we obtain: $\delta_1(\text{RT}) = 0.230$ mm/s and $\delta_2(\text{RT}) = -0.040$ mm/s . Hence, according to Eq. (1), the average Fe valence of the atoms in the sites 1 is 3.4, whereas the average Fe valence of the atoms in the less populated sites is 4.2. This CD qualitatively agrees with other techniques such as RXS and BVS but quantitatively is a bit higher maybe due to differences in the temperature dependence for δ_1 and δ_2 . In any case, this technique allows us to discard the occurrence of a full disproportionation in opposite to previous interpretations [19] but in agreement with recent reports [43].

D. Magnetic structure of $\text{Sr}_{2/3}\text{Pr}_{1/3}\text{FeO}_3$ and $\text{Sr}_{2/3}\text{Nd}_{1/3}\text{FeO}_3$

Previous studies have paid little attention to $\text{Sr}_{2/3}\text{Pr}_{1/3}\text{FeO}_3$ and $\text{Sr}_{2/3}\text{Nd}_{1/3}\text{FeO}_3$ in spite of these samples also exhibit a MIT and similar charge disproportionation. In fact, the magnetic ground state of these compounds is not well known so far. In this work we have characterized the magnetic arrangement of $\text{Sr}_{2/3}(\text{La}_{0.5}\text{Pr}_{0.5})_{1/3}\text{FeO}_3$, $\text{Sr}_{2/3}\text{Pr}_{1/3}\text{FeO}_3$, $\text{Sr}_{2/3}(\text{Pr}_{0.5}\text{Nd}_{0.5})_{1/3}\text{FeO}_3$, and $\text{Sr}_{2/3}\text{Nd}_{1/3}\text{FeO}_3$ to account for the effect of the rare earth size in the magnetic ordering of the Fe-sublattice. To determine it, we have proceeded in the same way as in the study of $\text{Sr}_{2/3}\text{La}_{1/3}\text{FeO}_3$. In this case, the low-temperature crystal structure adopts a monoclinic cell with space group $A2/n$. Magnetic reflections can also be

TABLE IV. Mössbauer spectral hyperfine parameters for $\text{Sr}_{2/3}\text{La}_{1/3}\text{FeO}_3$.

T (K)	Wt. Av. (%)	$\Gamma(\text{mms}^{-1})$	B_{hf} (T)	$\delta(\text{mms}^{-1})$	$\Delta E_Q, \varepsilon(\text{mms}^{-1})$
300	100	0.31	–	0.145	0.127
250	100	0.31	–	0.169	0.144
200	100	0.35	–	0.197	0.146
180	69	0.61	40.1	0.328	–0.008
	31	0.32	24.5	–0.034	–0.031
150	70	0.53	42.0	0.339	–0.009
	30	0.28	25.0	–0.034	–0.023
120	70	0.47	43.5	0.360	–0.015
	30	0.28	25.5	–0.031	–0.014
80	68	0.42	44.9	0.361	–0.017
	32	0.31	25.9	–0.030	–0.015

indexed with the propagation vector $\mathbf{k} = 0$. Exploring the possible magnetic structures, Isodistort program yields four mIrreps for this point, mGM1+ ($A2/n$), mGM2+ ($A2'/n'$), mGM1- ($A2/n'$), and mGM2- ($A2'/n$), which correspond to the magnetic groups indicated in parentheses for each mIrrep. In the last two groups, Fe atoms located at the Wyckoff position $4(d)$ do not participate in the magnetic arrangement

and therefore, they cannot account for the magnetic peaks observed in the neutron patterns at low temperature. The other two mIrreps, mGM1+ and mGM2+, allow the ordering associated to the sixfold periodicity (+ + + – – –). This ordering is only possible along the unique axis b in the magnetic group $A2'/n'$ (mGM2+), whereas it is allowed in the whole ac plane for the mGM1+. In this case, the refinements clearly show that the best fit is achieved when the magnetic moments lie along the c axis. Therefore, we have found two possible directions for the magnetic moments, either along the monoclinic b axis ($A2'/n'$) or the c axis ($A2/n$). In both cases, the moments are perpendicular to the monoclinic a axis, which corresponds to the body diagonal in the primitive cubic cell in the $A2/n$ cell choice. Therefore, the possible magnetic structures in the monoclinic ferrites are analogous to those observed in the trigonal $\text{Sr}_{2/3}\text{La}_{1/3}\text{FeO}_3$ and the difference comes from the different tilts of FeO_6 octahedra which lead to different unit cells. In the present work we report the results obtained in the $A2/n$ model (see Table III) but the magnitude of the ordered magnetic moments is similar using the $A2'/n'$ model and only changes its direction. In this case, the refinements using the $A2/n$ model give a little better reliability factors. This is a result similar to the La-based compound (magnetic ordering also perpendicular to the unique axis), but it is not the unique reason for this choice. The similar anomalies in the temperature dependences of their respective lattice parameters observed in Fig. 5 (a axis for La compound and c axis for Nd one) suggests similar magnetoelastic coupling at the magnetic transition coupled to the MIT. Figure 10 shows the magnetic ordering in these compounds and the refinements of the neutron patterns can be found in the Supplemental Material [31]. As can be seen in the Table III, the magnetic moments on Fe1 and Fe2 sites seem to be nearly independent of the substituted rare earth atom being the average magnetic moment for the Fe1 $\sim 2.54 \mu_B$, whereas for Fe2 is $\sim 3.37 \mu_B$. These values disagree with the expected moments for Fe^{5+} and Fe^{3+} and a diminution by covalence effects does not seem enough to justify this strong difference. On the other side, BVS indicates that both sites contain, as a first approximation, a mixture of Fe^{4+} and Fe^{3+} . Taking into account the octahedral coordination in both sites, Fe^{4+} is expected to show the low-spin (LS) configuration ($2 \mu_B$) as a strong distortion of the FeO_6 octahedron is required to stabilize the high-spin configuration [45]. Thus,

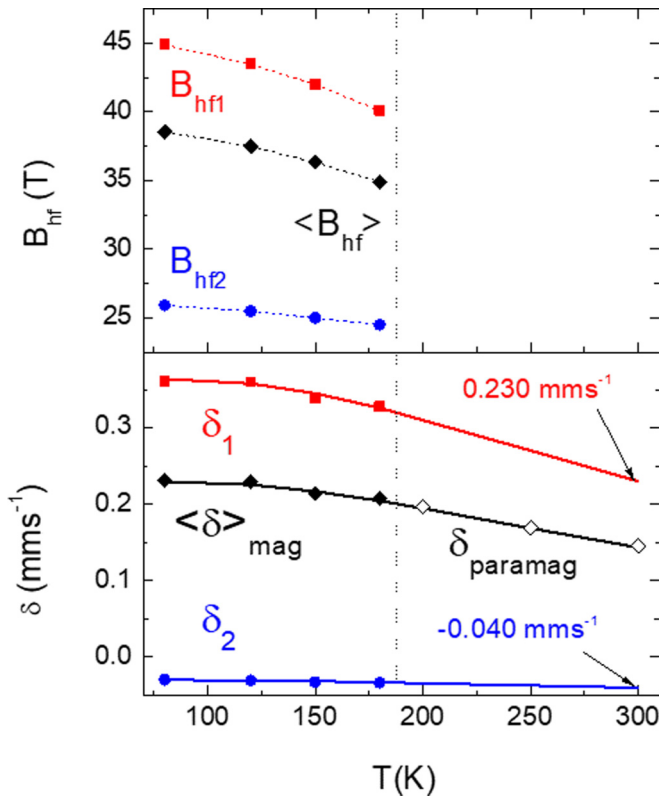


FIG. 9. Temperature dependence of the $\text{Sr}_{2/3}\text{La}_{1/3}\text{FeO}_3$ hyperfine magnetic field and isomer shift. The dotted line indicates the MIT temperature. In the magnetically split region ($T < T_{\text{MI}}$) the weighted averages: $\langle B_{\text{hf}} \rangle = 1/3 B_{\text{hf1}} + 2/3 B_{\text{hf2}}$ and $\langle \delta \rangle = 1/3 \langle \delta_1 \rangle + 2/3 \langle \delta_2 \rangle$ are also displayed. In the top panel the dashed lines are guides for the eyes. In the bottom panel the solid lines are the calculated (and extrapolated) thermal dependences of the isomer shift.

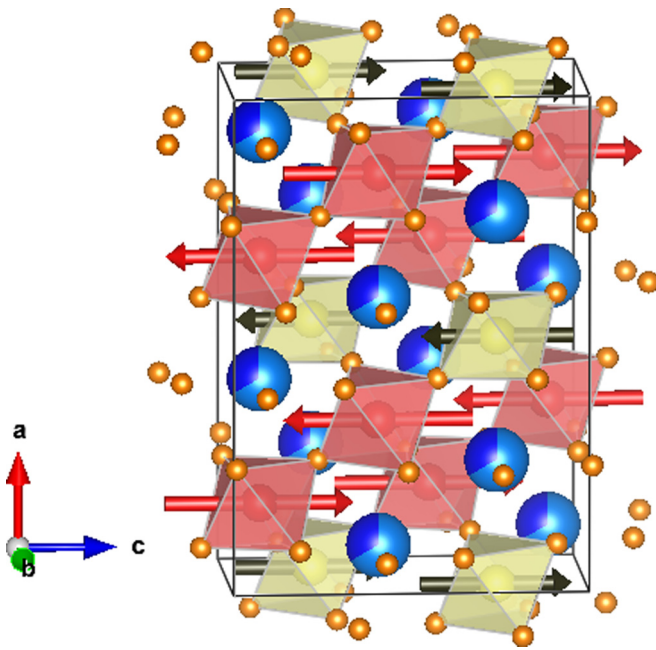


FIG. 10. Crystal and magnetic structure of $\text{Sr}_{2/3}\text{Ln}_{1/3}\text{FeO}_3$ ($\text{Ln} = \text{Pr}, \text{Nd}$) at 5 K deduced from the refinement of neutron diffraction patterns and a group-theoretical analysis. The draw was produced by VESTA program [41].

following an ionic approximation, the Fe1 site with $2.54 \mu_B$ may be composed by 82% of LS- Fe^{4+} and 18% of Fe^{3+} , whereas the Fe2 site would be occupied by 54% of LS- Fe^{4+} and 46% of Fe^{3+} . These cationic ratios agree reasonably well with the BVS obtained in the previous refinements using the model 1 (see Table II). In this way, it is worth remembering that superexchange rules [42] predict the same sign for $\text{Fe}^{5+}\text{-O-Fe}^{3+}$ and LS- $\text{Fe}^{4+}\text{-O-Fe}^{3+}$ interactions. In any case, the ionic approximation may be not adequate to explain the electronic properties of these compounds with Fe in high oxidation states. Spectroscopic studies revealed strong covalence and the ground state is better understood with ligand holes in the oxygen atoms [46]. In this way, oxygen atoms exhibit the longer shifts at T_{MI} . Analogously, soft x-ray absorption data on $\text{Sr}_{1-x}\text{La}_x\text{FeO}_3$ across T_{MI} revealed minor changes at the Fe L_3 -edge measurements whereas significant shifts are noticeable at the O K-edge spectra [47]. Phonon condensation at T_{MI} might relax structural strain in the environment of oxygen atoms and consequently, two nonequivalent Fe sites are formed developing a charge density wave (CDW) with a sixfold periodicity. The formation of this type of CDW is able to open a band gap as has been recently observed in the $\text{SrFeO}_{3-\delta}$ sample [48], very related to our compounds.

IV. CONCLUSIONS

The crystal structure at room temperature of $\text{Sr}_{2/3}\text{Ln}_{1/3}\text{FeO}_3$ compounds ($\text{Ln} = \text{La}, \text{Pr}$ and Nd) shows great similarities and the main difference is related to different rotation modes of FeO_6 octahedra. The hexagonal structure

of $\text{Sr}_{2/3}\text{La}_{1/3}\text{FeO}_3$ (space group $R\bar{3}c$) can be understood in the $a^-a^-a^-$ tilting system [30] whereas the monoclinic cell of $\text{Sr}_{2/3}\text{Pr}_{1/3}\text{FeO}_3$ and $\text{Sr}_{2/3}\text{Nd}_{1/3}\text{FeO}_3$ (space group $I2a$) corresponds to the $a^-a^-c^-$ set of tilts. This difference arises from the different strain induced by the different ionic size of Ln^{3+} cations. Despite of these differences, the three samples show a MIT at a similar critical temperature T_{MI} ranging between 195 and 180 K on heating.

Our comprehensive study using high-resolution x-ray powder diffraction, neutron diffraction, and Mössbauer spectroscopy has allowed us to gain significant insights into the crystal and magnetic structures below T_{MI} . Condensation of modes belonging to the Irrep LD1 in the primitive cubic cell associated to the vector $\mathbf{k} = (1/3, 1/3, 1/3)$ leads to a trigonal cell (space group $P\bar{3}c1$) for La-based sample and a large monoclinic cell (space group $A2/n$) for the other samples. The superstructure peaks are noticeable in the x-ray patterns using synchrotron radiation. In all cases, the low-temperature phase shows a sequence of expanded and compressed FeO_6 octahedra along a particular body diagonal in the primitive cubic cell with a ratio of 2:1. The atom shifts involved in the transition are so small that a minor CD is produced between two nonequivalent Fe sites in the low-temperature phase in agreement with the difference of about 0.4 valence units observed by the BVS method. Therefore, a full CD of Fe^{4+} into Fe^{3+} and Fe^{5+} is absolutely inadequate to account for the structural and magnetic changes observed at T_{MI} and this result concurs with previous RXS and x-ray absorption spectroscopy studies on $\text{Sr}_{2/3}\text{La}_{1/3}\text{FeO}_3$ [10,23]. The MIT is better explained in terms of the developing of a CDW in the Fe sublattice along a body diagonal in the primitive cubic cell that opens a band gap.

Coupled to the structural transition, long-range AFM ordering is established [38,43] with a similar sixfold periodicity. Refined magnetic moments for the two nonequivalent Fe sites were obtained from neutron diffraction patterns and its ratio was confirmed by Mössbauer spectroscopy. These moments disagree with a mixture of Fe^{3+} and Fe^{5+} cations and they are better accounted for by a mixture of LS- Fe^{4+} and Fe^{3+} moments. The use of a symmetry analysis helped us to determine the magnetic group for the magnetic arrangements and the most plausible direction of the magnetic moments as perpendicular to both, the unique monoclinic axis and the body diagonal where the CDW is established.

Summarizing, this study establishes that MIT in the $\text{Sr}_{2/3}\text{Ln}_{1/3}\text{FeO}_3$ system can be described as a structural phase transition where the condensation of modes mainly associated to oxygen atoms lead to two different iron sites, $\text{Fe}^{3.67+\delta}$ and $\text{Fe}^{3.67-\delta}$, with a ratio 1 to 2 and a total CD of about 0.4–0.6 electrons. Accordingly, a full CD with Fe^{5+} and Fe^{3+} cations is discarded.

ACKNOWLEDGMENTS

The authors acknowledge financial support from CICYT (Projects No. MAT2015-68760-C2-1 and No. MAT2014-54425-R) and DGA (Grant No. E69). We thank ESRF and ILL for granting beam time and Servicio General de Apoyo a la investigación from University of Zaragoza.

- [1] B. H. Savitzky, I. El Baggani, A. S. Admasu, J. Kim, S.-W. Cheong, R. Hovden, and L. F. Kourkoutis, *Nature Comm.* **8**, 1883 (2017).
- [2] M. Imada, A. Fujimori, and Y. Tokura, *Rev. Mod. Phys.* **70**, 1039 (1998).
- [3] S. Lafuerza, J. García, G. Subías, J. Blasco, and P. Glatzel, *Phys. Rev. B* **93**, 205108 (2016).
- [4] J. A. Alonso, J. L. García-Muñoz, M. T. Fernández-Díaz, M. A. G. Aranda, M. J. Martínez-Lope, and M. T. Casais, *Phys. Rev. Lett.* **82**, 3871 (1999); J. Blasco, M. Castro, and J. García, *J. Phys.: Condens. Matter* **6**, 5875 (1994).
- [5] E. J. W. Verwey, *Nature (London)* **144**, 327 (1939); J. García and G. Subías, *J. Phys. Condens. Matter* **16**, R145 (2004).
- [6] G. Subías, J. García, J. Blasco, J. Herrero-Martin, M. C. Sanchez, J. Orna, and L. Morellon, *J. Synch. Rad.* **19**, 159 (2012); G. Subías, J. García, and J. Blasco, *Phys. Rev. B* **71**, 155103 (2005).
- [7] Y. Sakai, K. Kaneda, N. Tsuda, and M. Tanaka, *J. Phys. Soc. Jap.* **55**, 3181 (1986).
- [8] M. Tanaka, J. Akimitsu, I. Inada, N. Kimuzuka, I. Shindo, and K. Siratori, *Solid State Commun.* **44**, 687 (1982); S. Lafuerza, G. Subías, J. Blasco, J. García, G. Nisbet, K. Conder, and E. Pomjakushina, *Europhys. Lett.* **107**, 47002 (2014).
- [9] P. D. Battle, T. C. Gibb, and P. Lightfoot, *J. Sol. State Chem.* **84**, 271 (1990).
- [10] J. Blasco, B. Aznar, J. García, G. Subías, J. Herrero-Martín, and J. Stankiewicz, *Phys. Rev. B* **77**, 054107 (2008).
- [11] J. Blasco, J. García, and G. Subías, *Phys. Rev. B* **83**, 104105 (2011).
- [12] J. García, G. Subías, M. G. Proietti, J. Blasco, H. Renevier, J. L. Hodeau, and Y. Joly, *Phys. Rev. B* **63**, 054110 (2001).
- [13] J. Blasco, S. Lafuerza, J. García, G. Subías, V. Cuartero, J. L. García-Muñoz, C. Popescu, and I. Peral, *Phys. Rev. B* **93**, 184110 (2016).
- [14] Y. Orikasa, T. Nakao, M. Oishi, T. Ina, A. Mineshige, K. Amezawa, H. Arai, Z. Ogumia, and Y. Uchimoto, *J. Mat. Chem.* **21**, 14013 (2011).
- [15] T. Das, J. D. Nicholas, and Y. Qi, *J. Mat. Chem. A* **5**, 25031 (2017).
- [16] D. Gryaznov, R. Merkle, E. A. Kotomina, and J. Maier, *J. Mat. Chem. A* **4**, 13093 (2016).
- [17] M. Lie, O. Nilsen, H. Fjellvåg, and A. Kjekshus, *Dalton Trans.* **3**, 481 (2009).
- [18] R. C. Devlin, A. L. Krick, R. J. Sichel-Tissot, Y. J. Xie, and S. J. May, *J. Appl. Phys.* **115**, 233704 (2014).
- [19] M. Takano, J. Kawachi, N. Nakanishi, and Y. Takeda, *J. Solid State Chem.* **39**, 75 (1981); J. Matsuno, T. Mizokawa, A. Fujimori, Y. Takeda, S. Kawasaki, and M. Takano, *Phys. Rev. B* **66**, 193103 (2002).
- [20] J. B. Yang, X. D. Zhou, A. Chu, W. M. Hikal, Q. Cai, J. C. Ho, D. C. Kundaliya, W. B. Yelon, W. J. James, H. U. Anderson, H. H. Hamdeh, and S. K. Malik, *J. Phys.: Condens. Matter* **15**, 5093 (2003).
- [21] P. M. Woodward, D. E. Cox, E. Moshopoulou, A. W. Sleight, and S. Morimoto, *Phys. Rev. B* **62**, 844 (2000).
- [22] J. Q. Li, Y. Matsui, S. K. Park, and Y. Tokura, *Phys. Rev. Lett.* **79**, 297 (1997).
- [23] J. Herrero-Martín, G. Subías, J. García, J. Blasco, and M. C. Sánchez. *Phys. Rev. B* **79**, 045121 (2009).
- [24] A. Mishra and S. Bhattacharjee, *J. Am. Cer. Soc.* **100**, 4945 (2017).
- [25] S. K. Park, T. Ishikawa, Y. Tokura, J. Q. Li, and Y. Matsui, *Phys. Rev. B* **60**, 10788 (1999).
- [26] J. Rodríguez-Carvajal, *Physica B* **192**, 55 (1993).
- [27] J. M. Perez-Mato, D. Orobengoa, and M. I. Aroyo, *Acta Cryst A* **66**, 558 (2010).
- [28] B. J. Campbell, H. T. Stokes, D. E. Tanner, and D. M. Hatch, *J. Appl. Crystallogr.* **39**, 607 (2006); available at ISOTROPY Software Suite, iso.byu.edu.
- [29] D. Orobengoa, C. Capillas, M. I. Aroyo and J. M. Perez-Mato, *J. Appl. Crystallogr.* **42**, 820 (2009).
- [30] V. M. Goldschmidt, *Die Naturwissenschaften.* **14**, 477 (1926).
- [31] See Supplemental Material at <http://link.aps.org/supplemental/10.1103/PhysRevB.98.104422> for description of the relationships between crystal structure and octahedra tilts for ordered and disordered perovskites. Relationship between parent and distorted structures with the corresponding transformation matrices. Plots of the refinements of neutron diffraction patterns for all samples. Plots of the Mössbauer spectra for reference compounds and the linear relationship obtained for the isomer shift vs. Fe valence at room temperature
- [32] A. M. Glazer, *Acta Cryst. A* **31**, 756 (1975).
- [33] P. M. Woodward, *Acta Cryst. B* **53**, 32 (1997).
- [34] C. J. Howard and H. T. Stokes, *Acta Cryst. B* **54**, 782 (1998).
- [35] P. W. Stephens, *J. Appl. Crystallogr.* **32**, 281 (1999).
- [36] Y. R. Uhm, S. W. Lee, k.-T. Park, Y. Tomioka, Y. Tokura, and C. S. Kim, *J. Appl. Phys.* **87**, 4873 (2000).
- [37] R. Kajimoto, Y. Oohara, M. Kubota, H. Yoshizawa, S. K. Park, Y. Taguchi, and Y. Tokura, *J. Phys. Chem. Solids* **62**, 321 (2001).
- [38] J. Blasco, M. C. Sánchez, J. García, J. Stankiewicz, and J. Herrero-Martin, *J. Cryst. Growth* **310**, 3247 (2008).
- [39] M. Stange, J. Lindén, A. Kjekshus, N. Binsted, M. T. Weller, B. C. Hauback, and H. Fjellvåg, *J. Sol. State Chem.* **173**, 148 (2003).
- [40] C. J. Howard and H. T. Stokes, *Acta Cryst. B* **60**, 674 (2004).
- [41] K. Momma and F. Izumi, *J. Appl. Crystallogr.* **44**, 1272 (2011).
- [42] J. B. Goodenough, *J. Phys. Chem. Solids* **6**, 287 (1958); J. Kanamori, *ibid.* **10**, 87 (1959).
- [43] F. Li, V. Pomjakushin, T. Mazet, R. Sibille, B. Malaman, R. Yadav, L. Keller, M. Medarde, K. Conder, and E. Pomjakushina, *Phys. Rev. B* **97**, 174417 (2018).
- [44] G. J. Long, D. Hautot, F. Grandjean, D. T. Moreli and G. P. Meisner, *Phys. Rev. B* **60**, 7410 (1999); R. H. Herber, *1984 Chemical Mössbauer Spectroscopy*, edited by R. H. Herber (Plenum, New York, 1984), p. 199.
- [45] G. Demazeau, M. Puchard, N. Chevreau, M. Thomas, F. Menil, and P. Hagenmuller, *Mater. Res. Bull.* **16**, 689 (1981).
- [46] S. Nasu, T. Kawakami, S. Kawasaki, and M. Takano, *Hyperfine Interact.* **144/145**, 119 (2002).
- [47] H. Wadati, A. Chikamatsu, R. Hashimoto, M. Takizawa, H. Kumigashira, A. Fujimori, M. Oshima, M. Lippmaa, M. Kawasaki, and H. Koinuma, *J. Phys. Soc. Jap.* **75**, 054704 (2006).
- [48] S. H. Hsieh, R. S. Solanki, Y. F. Wang, Y. C. Shao, S. H. Lee, C. H. Yao, C. H. Du, H. T. Wang, J. W. Chiou, Y. Y. Chin, H. M. Tsai, J.-L. Chen, C. W. Pao, C.-M. Cheng, W.-C. Chen, H. J. Lin, J. F. Lee, F. C. Chou and W. F. Pong, *Sci. Rep.* **7**, 161 (2017).